Research Square

Preprints are preliminary reports that have not undergone peer review.
They should not be considered conclusive, used to inform clinical practice,
or referenced by the media as validated information.

The mechanistic aspects of chloride-induced stress corrosion cracking and internal pitting in stainless steel

Ronit Roy

ronitroy@illinois.edu

University of Illinois

Johan E. Westraadt

The Ohio State University

Janelle P. Wharry

University of Illinois

Article

Keywords: CISCC, Internal pits, Austenitic stainless steels, HR-EBSD, controlled ECCI, Schmid Factor

Posted Date: August 14th, 2026

DOI: https://doi.org/10.21203/rs.3.rs-10491066/v1

License: This work is licensed under a Creative Commons Attribution 4.0 International License.
Read Full License

Additional Declarations: Competing interest reported. The authors declare that they have no known competing financial interests that could have influenced the work. Janelle P. Wharry is a Guest Editor for the Environmentally Assisted Fracture Collection at npj Materials Degradation.

The mechanistic aspects of chloride-induced stress corrosion cracking and internal pitting in stainless steel

Ronit Roy[1]✉, Johan E. Westraadt[2], Janelle P. Wharry[1]✉

[1] Department of Mechanical Science & Engineering, University of Illinois, Urbana, IL, USA

[2] Center for Electron Microscopy and Analysis, The Ohio State University, Columbus, OH, USA

Corresponding authors:

✉ ronitroy@illinois.edu (Ronit Roy)

✉ jpw@illinois.edu (Janelle P. Wharry)

The objective of this study is to understand the mechanistic drivers of chloride-induced stress corrosion cracking (CISCC). CISCC is a critical degradation mode in structural alloys exposed to chloride-rich environments, so understanding its deformation mechanisms is essential for the design and safe operation of these alloys. Although numerous studies have examined CISCC behavior, most have focused on electrochemical processes, leaving the mechanics of CISCC poorly understood. In this study, the deformation mechanisms of CISCC in austenitic stainless steel are investigated using high-angle-resolution electron backscatter diffraction (HR-EBSD) and controlled electron channeling contrast imaging (cECCI). The deformation fields along crack paths, near crack tips, and around internal pits are investigated in terms of residual elastic fields, GND density, and

dislocation imaging. Results show that CISCC is highly sensitive to grain-scale plasticity, i.e., the availability of slip systems in a given grain. CISC cracks propagate through high-Schmid-factor grains via extensive plasticity, while they propagate through lower-Schmid-factor grains in close alignment with the {111} planes with minimal plasticity. Characteristic peanut-shaped plastic zones, along with mixed-mode cracking, are observed, analogous to mechanically driven cracks. In addition, the formation of internal pits, a newly emergent phenomenon in CISCC, is determined to be caused by stepwise crack propagation during brittle fracture promoted by localized accelerated corrosion at the crack tip. Using state-of-the-art characterization of deformation fields, this study develops the mechanistic underpinnings of CISC crack propagation and internal pitting, which can be used to engineer grain-orientation-based CISCC resilience in structural alloys.

Keywords

CISCC, Internal pits, Austenitic stainless steels, HR-EBSD, controlled ECCI, Schmid Factor

Austenitic stainless steels are extensively used as structural alloys across numerous industries, owing to their superior mechanical performance and corrosion resistance[1,2]. One of the critical material challenges associated with austenitic stainless steels is their susceptibility to stress corrosion cracking (SCC)[3]. SCC leads to rapid cracking and failure of structural alloys, often without enough prior indications[4,5]. Typically, various grain boundary engineering techniques, such as low-carbon alloying, are utilized to mitigate SCC in austenitic stainless steels[6]. However, such grain boundary engineering predominantly controls intergranular SCC (IGSCC), whereas transgranular SCC (TGSCC) persists as an active failure mode even in grain boundary-engineered austenitic stainless steels[7,8]. The TGSCC in austenitic stainless steels is more pronounced in chloride-rich environments (such as coastal regions), even at standard atmospheric conditions with minimal stresses[9], thus typically referred to as chloride-induced SCC (CISCC). During CISCC, corrosion pits form initially at the exposed surface of the material, and transgranular cracks initiate from these pits and propagate further into the material under applied or residual tensile stresses[9–12]. Degradation by CISCC in austenitic stainless steels is evident in numerous industries, such as oil and gas[13,14] and nuclear power[15]. An instance of CISCC in the nuclear industry occurs in spent nuclear fuel (SNF) canisters, which are often stored in coastal environments for natural cooling. The combination of the coastal environment and weld-induced residual tensile stresses in the material paves the way for chloride-induced stress corrosion (CISC) cracks to initiate along arc-weld seams in SNF canisters. Thus, CISCC has emerged as a likely and critical degradation mechanism in SNF canisters[16–18]. Hence, understanding the CISCC

behavior in austenitic stainless steel is essential for accurately assessing material integrity and lifetime, thereby ensuring the safe design of nuclear waste storage facilities.

Pitting and crack initiation during CISCC are primarily influenced by the corrosive environment[16,19]. A comprehensive review of CISCC in austenitic stainless steels, focusing on the environmental conditions, is reported by Xie and Zhang[17]. Alongside this, the work by Qu et al. provides an overview of CISCC behavior in regard to SNF applications, emphasizing the CISCC mechanism and its mitigation strategies[18]. Note that most of the works to date relevant to CISCC in austenitic stainless steels have focused on corrosion, whereas works focused on the mechanics of CISCC are limited. Indeed, corrosion initiates pits that transition into cracking[20], but subsequent crack propagation is governed by stresses[9,21,22]. Therefore, a mechanistic understanding of the CISCC is necessary to fully understand material degradation behavior. Recent works on CISCC mechanics include Schoell et al.[21,22], which investigated the effect of stress on CISC crack propagation behavior. The role of microstructure on the CISCC has been reported by Qu et al.[9], who observed that grain hardness significantly influences crack propagation behavior. Evidence of strain-induced α'-martensitic transformation during CISCC in austenitic stainless steels has been shown[23–25]. Recently, the origin of the strain-induced α'-martensitic transformation during CISCC has been demonstrated and correlated with the microstructure[26]. However, the aforementioned works primarily focus on microstructural characterization and its effects on the CISC crack propagation behavior. Hence, a direct correlation of CISCC with the effective

strain/deformation fields is somewhat underdetermined. In this work, we aim to bridge this gap using high-resolution electron backscatter diffraction (HR-EBSD) and electron channeling contrast imaging (ECCI) techniques.

HR-EBSD is a non-destructive surface characterization technique performed with scanning electron microscopes (SEM)[27,28]. HR-EBSD measures small changes in Kikuchi band positions relative to a reference Kikuchi pattern using an FFT-based cross-correlation technique and calculates the deformation gradient tensor[29,30]. By decomposing this deformation gradient tensor, the elastic and rotation tensors are estimated with an accuracy of 10^{-4} and 10^{-4} rads, respectively[27,30]. Alongside, deformation fields ranging from tens to hundreds of microns can be mapped in sub-micron resolution with HR-EBSD[31]. HR-EBSD has been used to estimate microscale crack tip deformation fields[32–35] and microstructural characteristics in materials relevant to nuclear applications[36–38]. Alternatively, controlled electron channeling contrast imaging (cECCI) is a non-destructive, SEM-based technique in which the specimen is tilted to place the grain of interest into a two-beam diffraction condition relative to the primary electron beam[39,40]. The strain fields exerted by the dislocations (or defects) locally perturb the lattice and change the Bragg's diffraction conditions for backscattered electrons (BSE), generating diffraction contrast, which enables dislocation (or defect) imaging at the grain scale. In this study, HR-EBSD and cECCI are used to characterize crack tip deformation fields, which are then correlated with CISC crack propagation behavior to evaluate the CISCC mechanisms in austenitic stainless steels. To the best of the author's knowledge, this is the first attempt to describe the CISCC phenomenon in a truly mechanistic way.

The objective of the present study is to investigate deformation characteristics during CISCC in austenitic stainless steels and illustrate the crack propagation behavior. In addition, we demonstrate the origin of internal pits along the crack path as a function of microstructure and crack propagation behavior. In the present study, a 304L stainless steel specimen with a central arc weld is used to mimic the longitudinal weld seams in SNF canisters susceptible to CISCC. The CISCC mechanism is investigated across two different CISC crack configurations: (1) into lower Schmid factor grains and along grain boundaries (brittle fracture), and (2) into higher Schmid factor grains (ductile fracture). A combination of HR-EBSD analysis and cECCI is used to characterize deformation fields, estimate residual elastic fields, determine geometrically necessary dislocation (GND) density, and image dislocations. These results will be used to explain the mechanistic aspects of CISCC.

Results

HR-EBSD and cECCI results obtained at different CISC cracked regions are presented in this section. First, crack propagation behavior through lower Schmid factor grains and along grain boundaries (i.e., intergranular cracks) is shown. Subsequently, crack propagation behavior through grains with higher Schmid factors is presented.

Lower Schmid factor grains, grain boundaries, internal pitting

At first, a transgranular crack propagating through a lower Schmid factor grain is analyzed. A secondary electron image of the cracked region is shown in Fig. 1(a). The crystallographic orientation of the region is shown in Fig. 1(b) as an inverse

pole figure (IPF) map along the Z-axis (parallel to the TD of the sample), while Fig. 1(c) shows the Schmid factor map of the region. As the specimen is subjected to pure bending, a $[100]$ stress vector along its longitudinal direction (LD), which replicates the only tensile stress, is used for all Schmid factor analyses presented in this work[41]. The estimate shows that the cracked grain has a Schmid factor of 0.45, as denoted in the figure. We note that at the microscale, localized stresses resulting from the grain structure are significantly more complex than the pure bending assumption. However, as we only focus on the relative grain plasticity, i.e., harder or softer grains, this approximation does not alter the present observations. The HR-KAM map shown in Fig. 1(d) represents the plastic strain gradient in the material. We note that all HR-KAM maps presented in this study are estimated using nearest-neighbor approximation, excluding the diagonal pixels[34]. On crack edges (along the crack path), significantly higher HR-KAM values are observed compared to the rest of the grain. This represents a significant change in the plastic strain field along the crack path resulting from crack propagation. On the other hand, HR-KAM values around the internal pit (bottom-right corner of the mapped region) are similar to those of the rest of the grain, indicating no evidence of significant plastic deformation around the pit. In this work, the GND density is estimated using Nye's tensor framework[42] with 'L-1 energy minimization'[43,44]. All possible dislocation types in face-centered cubic (FCC) materials are used for the GND density analysis. Fig. 1(e) exhibits the total GND density map at the cracked region. Similar to the HR-KAM, a higher GND density is observed along the crack edges, showing significant plastic deformation resulting from crack propagation. A narrow GND density band is also

observed at the bottom-right internal pit. However, as the GND density map is presented in logarithmic scale, the difference in GND density between the crack edge and the pit edge is substantial.

To further investigate the dislocation microstructure that evolved around the crack edge and internal pit edge, cECCI has been used. Fig. 2(a) exhibits the ECC image corresponding to the crack tip presented in Fig. 1, where the cracked grain is under a two-beam condition. Further, higher magnification ECC images at the crack edge and pit edge are shown in Fig. 2(b) and 2(c), respectively. We note that backscatter electrons can escape from the edges of the material, resulting in brighter edges in cECCI than the rest of the grain[39], as seen in Fig. 2(a). To enhance the dislocation image quality, these edges are masked in all higher-magnification ECC images in this study. Similar to the HR-KAM and GND density maps, significant dislocations are observed at the crack edges, shown in light contrast in Fig. 2(b). In comparison, fewer dislocations are observed at the internal pit edges in Fig. 2(c), specifically at the bottom-left corner of the map, indicating pit growth driven by corrosion mechanisms.

Fig. 3 shows the spatial distribution of the residual elastic strain tensor estimated using HR-EBSD analysis in the cracked region from Fig. 1. The HR-EBSD analysis axis convention is also shown. Axis 1 in the strain maps is parallel to the tensile stress direction resulting from pure bending. Whereas axes 2 and 3 correspond to the crack propagation direction and the out-of-plane direction, respectively. All residual elastic strain maps presented here are screened using geometric mean peak height (pH) and mean angular error (MAE) of the HR-EBSD analyses to ensure measurement accuracy [45,46]. All residual elastic strains

estimated in this study are relative to each grain, owing to the limitation of absolute strain measurements in the HR-EBSD analysis[47,48]. Across strain maps, a significant elastic strain localization is observed along the crack edges, representing significant elastic deformation in the region. In contrast, the residual elastic strain at the bottom-right internal pit edge is significantly lower than that observed at the crack edge and is only restricted to the normal components of the strain tensor. This represents minimal distortion of the crystal lattice at the internal pit edges. In addition, a higher concentration of residual elastic strains is observed at the crack tip and the lower-right corner of the top-left grain. This indicates the crack tip field remains in an elastic deformation regime, as no corresponding deformation concentrations are observed in the HR-KAM and GND density maps.

One might argue that rounding off crack edges during sample preparation could affect HR-EBSD analysis and result in higher elastic strains, HR-KAM, and GND density at those crack edges, much like the brighter crack edges in the ECC images. But HR-EBSD analyzes Kikuchi patterns, in which bands form due to the coherent scattering of electrons from crystallographic planes. Hence, rounding off crack edges may change the electron yield from the region, but does not alter the Kikuchi band locations. One could also argue that any deformation during edge rounding can lead to spurious deformation fields near the edges. But such deformation fields would be comparable between crack edges and internal pits, whereas the present data show significant differences in elastic strains, HR-KAM, and GND density across these features (implying these are real differences).

Therefore, the current HR-EBSD results are free of errors due to possible edge rounding during sample preparation.

Next, an example of intergranular crack propagation during CISCC is shown in Fig. 4, which is comparable to brittle crack propagation. Fig. 4(a) shows the secondary electron image taken at the cracked region. The IPF map along the Z-axis in Fig. 4(b) shows the crystallographic orientation information of the cracked region. The corresponding Schmid factor map is shown in Fig. 4(c). The top-left grain near the crack tip/triple point has a Schmid factor of 0.34, also indicated in the figure. The HR-KAM map is shown in Fig. 4(d). Higher HR-KAM values are restricted to the crack edges, identical to the previous example. In addition, higher HR-KAM values are also observed at grain boundaries and the triple point near the crack tip. The GND density is shown in Fig. 4(e). Similar to HR-KAM, higher GND density is observed at the crack edges and at grain boundaries/triple points ahead of the crack tip, indicating significant plastic deformation in those regions. In addition, GND density is also observed at the edges of the internal pit, although the magnitude is less than that observed at the crack edge/tip regions.

The dislocation microstructure evolved in the top-left grain adjacent to the crack tip (corresponding to the intergranular crack in Fig. 4 with a Schmid factor of 0.34) is characterized using cECCI and shown in Fig. 5(a). To further investigate the dislocation structure at the crack tip, higher-magnification images from the grain of interest are shown in Figs. 5(b), and 5(c). In addition, the dislocation microstructure in a grain further away from the crack tip is shown in Fig. 5(d), representing the residual dislocation density in the material, which does

not result from cracking. A significantly higher dislocation density is observed in the crack tip grain compared to the reference grain (Fig. 5(d)), which indicates plastic deformation resulting from the crack tip fields.

The spatial distribution of the residual elastic strains around the intergranular crack is shown in Fig. 6. Across the strain maps, elastic strain localization is observed along the crack path, representing elastic deformation in the region. More interestingly, significant elastic strain concentrations are observed at grain boundaries and triple points ahead of the crack tip, suggesting substantial elastic deformation in that region, comparable to the GND density map and cECCI analysis. Apart from that, the strain concentrations along the internal pit edges are comparatively lower than those observed at the crack edge/tip regions, similar to the internal pit edges of the first example (refer to Fig. 3). We note that the uniform residual elastic strain distribution on the grain right side of the crack is either result from selection of the reference patterns or the presence of a minute orientation gradient in the grain, as such deformation is not characteristic of the localized crack tip fields.

Another example of transgranular crack propagation through a lower Schmid factor grain, containing an internal pit along the crack path, is shown in Fig. 7. A secondary electron image of the cracked region is shown in Fig. 7(a). The crystallographic orientation information of the cracked region is shown in Fig. 7(b), as an IPF map along the Z-axis. Fig. 7(c) shows the Schmid factor map. The estimate shows that the cracked grain has a Schmid factor of 0.38, as indicated in the figure. We note that the two small triangular grains at the top-right corner and the bottom-middle region are residual δ-ferrite phase retained from heat

treatment or welding[26]. The HR-KAM map of the cracked region is shown in Fig. 7(d). As in the previous two examples, the higher HR-KAM values are concentrated only at the crack edges. Distribution of HR-KAMs is also observed at the tips of δ-ferrite phases, resulting from deformation incompatibility between phases. In fact, the line concentration from the bottom-middle δ-ferrite phase perhaps suggests the formation of a secondary crack, which is somewhat visible in the secondary electron image. Apart from that, the HR-KAM at the internal pit edges is not elevated compared to the rest of the grain. The GND density map estimated at the cracked region is shown in Fig. 7(e). Higher GND density is observed at the crack edges and the phase boundaries, whereas the GND density specifically at the left side of the internal pit is significantly lower. For brevity, the cECCI and residual elastic strain analyses for the present dataset are not included, as the dataset yields results similar to those of the first two crack examples.

Higher Schmid factor grains, plastic deformation

Transgranular crack propagation through a higher Schmid factor grain with the crack tip reaching a grain boundary is presented in Fig. 8. The secondary electron image of the transgranular crack example is shown in Fig. 8(a). The crystallographic orientation information of the crack region is presented as an IPF map along the Z-axis in Fig. 8(b). The Schmid factor map is shown in Fig. 8(c). The analysis estimates Schmid factors of 0.48 in the bottom cracked grain and 0.43 in the grain ahead of the crack tip, as marked in the figure. The bottom (magenta) grain has a slightly different Schmid factor on either side of the crack, resulting from rotation of the region due to crack opening. This bottom grain, in

which the crack has already propagated, has a higher Schmid factor, facilitating large plastic deformation within the grain. Fig. 8(d) exhibits the HR-KAM map estimated from the cracked region. Regions near the crack tip, crack edges, and some in-grain pixels undergo significant plastic deformation, which has been removed from the current dataset due to poor Kikuchi pattern quality; these pixels appear as white in the HR-KAM and GND density maps. Higher HR-KAM values are observed near the crack edges in the bottom grain, indicating significant plastic deformation in this region. Notably, despite being a lower Schmid factor grain, the top grain ahead of the crack tip also exhibits significant plastic deformation. The GND density map at the cracked region is shown in Fig. 8(e). Similar to HR-KAM maps, significant GND density is observed throughout the crack tip region. Interestingly, GND density ahead of the crack tip shows a characteristic peanut-shaped plastic zone associated with a mode I crack.

The dislocation microstructure that evolves during crack propagation is analyzed by cECCI and presented in Fig. 9. A backscatter electron image at the crack tip region (corresponding to the crack presented in Fig. 8) is shown in Fig. 9(a). High-magnification ECC images taken ahead of the crack tip in the lower Schmid factor grain are shown in Fig. 9(b). Apart from the very bright edges of the crack tip (an artifact of the escape of backscatter electrons), the smeared bright contrast at the left side of the crack tip indicates significant plastic deformation and lattice distortion, as also observed in the HR-KAM and GND density maps. Activation of two distinct slip systems is observed ahead of the crack tip, with a characteristic peanut-shaped plastic zone. We note that this occurs in a relatively lower Schmid factor grain in the present example. A higher-

magnification ECC image along the crack edge in the higher Schmid factor grain is shown in Fig. 9(c). Alongside smeared bright contrast, a significant number of dislocations is observed, indicating substantial plastic deformation along the crack edge. Owing to the high plastic deformation associated with crack propagation through grains with higher Schmid factors, no residual elastic strain analysis can meaningfully be conducted for the current dataset.

Another example of transgranular crack propagation through a higher Schmid factor grain is shown in Fig. 10. A secondary electron image of the cracked region is presented in Fig. 10(a). The crystallographic orientation information of the cracked region is shown in Fig. 10(b), as an IPF map along the Z-axis. Fig. 10(c) shows the Schmid factor map of the cracked region, with austenite grains exhibiting a Schmid factor of 0.49. The HR-KAM and GND density maps estimated from the present cracked region are shown in Figs. 10(d) and 10(f), respectively. We note that the bottom-right side of the crack tip is subjected to high plastic deformation and strain-induced martensite transformation[26] and is therefore omitted from the present HR-KAM and GND density analyses (appears as white pixels). In addition, some pixels at the crack tip are also removed owing to the high plastic deformation and poor Kikuchi pattern quality. Compared to the characteristic peanut-shaped plastic zone in the previous crack example, a somewhat less pronounced asymmetric peanut-shaped plastic zone is observed at the crack tip in both HR-KAM and GND density maps. Interestingly, the remaining plastic deformation field is confined to the crack edges, unlike in the previous example. This is likely because most of the

deformation associated with the crack propagation accommodates the strain-induced martensite transformation.

To further investigate the extent of the strain-induced martensite transformation, high spatial resolution electron backscatter diffraction (EBSD) is presented in Fig. 11. The phase map obtained in the cracked region is shown in Fig. 11(a). The crystallographic orientation of the cracked region is shown in Fig. 11(b), as an IPF map along the Z-axis. Fig. 11(c) shows the Hough transform confidence index (cutoff value: 0.1), indicating the reliability of the indexing. We note that the phase transformation in the region is not due to heat treatment or welding, as the cracks propagate through the outer heat-affected zone, where the microstructure is indistinguishable from that of the base metal.

Discussion

The results presented in this work demonstrate that CISC crack propagation behavior is strongly related to grain-scale plasticity. Despite using the simplified uniaxial stress vector, the dislocation microstructure that evolves during CISC cracking is consistent with Schmid factor analysis.

In examples where crack propagation occurred through lower Schmid factor grains (Schmid factor ≤ 0.45), the crack-induced dislocation microstructure is primarily restricted near the crack edges. Whereas, the rest of the grain(s) remain similar to the pre-deformed microstructure. This suggests minimal plastic deformation during CISC crack propagation in lower Schmid factor grains. We note that the absolute Schmid factor range in the test material is relatively low, reflecting the high number of slip systems in FCC, which range from ~0.4 to 0.5[9].

So, the relative difference is quite significant within this range. Moreover, the crack propagation paths are straight and in close alignment with the $\{111\}$ plane, as shown in Figs. 1 and 2. Similar stress corrosion cracks along $\{111\}$ planes have been reported in austenitic stainless steels[10,49]. We note that in a perfect brittle fracture, no plastic deformation is expected along the crack edges. However, in practice, some plastic deformation is inevitable, leading to extremely localized plastic deformation fields restricted to crack edges. Such localized plastic deformation fields are negligible compared to a ductile crack. Therefore, grains with lower Schmid factors are more prone to brittle fracture during CISCC.

On the other hand, CISC crack propagation through grains with higher Schmid factors (Schmid factor ≥ 0.48) results in significant plastic deformation across grains. For the crack example shown in Fig. 8, the GND density is distributed far from the crack edges. The extent of GND density distribution is ~4.5 μm on the left side of the crack and ~3.9 μm on the right side of the crack, and is distributed through multiple grains. This demonstrates the extent of plastic deformation associated with the CISC crack in a higher Schmid factor - plastic grain, which is comparable to the ductile fracture phenomenon.

Interestingly, even with extensive plasticity in this higher Schmid factor grain, a characteristic peanut-shaped GND density distribution is observed in the relatively lower Schmid factor grain above it (i.e., the grain with a Schmid factor of 0.43 into which the crack appears to be propagating, in Fig. 8(e)). This observation suggests plastic deformation occurs in that relatively lower Schmid factor grain, which can be attributed to two factors. First, this higher crack tip plastic deformation results from the CISC crack pausing at the grain boundary

before propagating into a lower Schmid factor grain. This is consistent with the characteristic of crack propagation: unlike plastic cracks, brittle cracks tend to propagate rapidly but may pause intermittently until they reach the critical stress intensity factor required for further growth[2,50,51]. Secondly, as the CISC crack has not yet propagated through the lower Schmid factor grain, no release of strain energy has occurred through surface creation, relaxation of elastic strain, and/or dislocation annihilation at the crack tip[52]. The GND density is therefore a result of the strain accumulation at the crack tip before entering the lower Schmid factor grain. Despite having comparable GND distribution in both higher and lower Schmid factor grains (see Fig 8(e)), the dislocation microstructure in the ECC images shows a significant difference in dislocation density between these two grains. The lower Schmid factor grain (see Fig. 9(b)) shows an overall lower dislocation density than the higher Schmid factor grain (see Fig. 9(c)), where most of the dislocations are distributed only in the vicinity of the crack tip. This suggests that plastic deformation in the lower Schmid factor grain is accommodated by strain gradients and lattice rotations, which are attributed to slip systems that are less favorably oriented.

Greater plastic deformation is also observed in the CISC crack example given in Fig. 10. Here, the CISC crack propagates through a higher Schmid factor grain, and upon intersecting a low-angle grain boundary, the crack kinks parallel to the low-angle grain boundary. The asymmetric peanut-shaped distribution of GND density at the crack tip represents characteristic mixed-mode cracking[53]. A greater plastic deformation field is observed at the obtuse-angle edge at the

bottom of the kink point, leading to a strain-induced martensite transformation in the region[26].

Overall, the results suggest that CISC crack propagation behavior is strongly dependent on grain-scale plasticity. Depending on the Schmid factor of a grain, CISC crack propagation behavior can be brittle or ductile. Moreover, the peanut-shaped deformation fields and mixed-mode cracking indicate that CISC cracks are comparable to mechanically driven cracks and are consistent with conventional fracture mechanics.

A recent study on CISCC in austenitic stainless steels has reported the formation of internal pits along the CISC crack path[54]. In that work, it is notable that although multiple pits form within a complex branched crack, not all branches and not all grain boundaries develop a pit. Hence, the origin of these internal pits remains unclear. Here, we demonstrate the conditions under which internal pits may form using a mechanistic approach.

In the present study, internal pits form only along CISC crack segments that undergo brittle fracture, i.e., in the lower Schmid factor grain. We postulate that the formation of internal pits is correlated with crack propagation behavior. The absence of sufficient slip systems in low Schmid factor grains limits the ability to relieve crack tip stresses through slip activation. Thus, the crack tip stresses are resolved only by creating new surfaces, thereby accelerating crack propagation at a faster rate than in higher Schmid factor grains[50,55]. However, such brittle cracks typically propagate in a stepwise manner under subcritical crack growth, pausing intermittently if they have not reached the critical stress

intensity factor for further growth[2,50,51]. Crack propagation can resume only when the applied stress intensity factor reaches the critical value for further propagation.

The formation of internal pits can be correlated with this stepwise propagation of brittle cracks. While propagation is paused, the crack tip stresses cause plastic deformation at the crack tip (see the crack tip in Fig. 4(e)), which exceeds the localized plastic deformation along the brittle crack edges (see Figs. 1(e) and 4(e)). Thus, greater crack tip plasticity results in a higher dislocation density in its vicinity, which can then promote localized accelerated corrosion while crack propagation is paused[56,57]. Ultimately, this process leads to the formation of internal pits along the brittle crack path. The HR-EBSD and cECCI analyses presented in this study also reveal significant differences in the dislocation microstructure between the crack edge and the internal pit edges, suggesting that the pit edges are formed by a corrosion-driven mechanism rather than stress-driven fracture.

One can make the counterargument that once an internal pit forms at the crack tip, the larger crack tip opening displacement would prevent rapid further crack growth and alter crack propagation toward a more ductile mode. Indeed, the formation of internal pits at the crack tip would further reduce the stress intensity factor. But the lack of slip systems in a lower Schmid grain would be unable to resolve the crack tip stresses and thereby prevent the crack from changing to a ductile mode. Thus, the formation of internal pits would lengthen the pause time between crack propagation steps, thus allowing more time for localized corrosion. This is consistent with the crack tip example shown in Fig. 1,

where the crack tends to propagate in a brittle manner following a close alignment with the {111} planes between any two internal pits (whereas a change in fracture mode would have altered the crack path).

We note that the origin of internal pitting in austenitic stainless steels during CISCC may not be exclusive to grain-scale plasticity examined in this study. In addition, multiple mechanisms have been proposed for surface pitting and surface pit-to-crack transitions, which could also play a role in internal pitting. Further assessments are warranted to understand the competition and interplay between CISCC propagation and internal pitting, in order to engineer grain orientations and texture that are inherently more resilient to CISCC.

In summary, CISCC is a critical degradation mode for structural alloys operating in a chloride-rich environment. Understanding CISCC mechanisms is therefore essential for the design and safe operation of such alloys. The present study investigates how the availability of slip systems at the grain level alters CISCC. For this purpose, the CISCC in austenitic stainless steels is simulated using boiling $MgCl_2$ immersion. Further, the crack propagation behavior is investigated using HR-EBSD and cECCI analyses. These advanced characterization approaches enable elucidation of the mechanics of CISC cracks that could not previously be identified directly. In addition, the origins of the newly reported phenomenon of internal pitting along brittle segments of CISC cracks are also revealed.

The CISC crack propagation behavior is strongly dependent on grain-scale plasticity and significantly differs between grains with higher compared to lower

Schmid factors. CISCC can be brittle or ductile, depending on the Schmid factors of the grain through which the crack is propagating.

- In higher Schmid factor (≥ 0.48) grains, the CISC crack-induced dislocation microstructure persists far from the crack edges, even into neighboring grains, resulting in an extended plastic deformation field. Evidence of strain-induced martensite transformation is also observed in a grain with a higher Schmid factor, indicating significant plastic deformation in the region. These findings corroborate the ductile CISC crack propagation behavior in higher Schmid factor grains.
- By contrast, in lower Schmid factor (≤ 0.45) grains, plastic fields are observed only locally along the crack edges, while the rest of the grain remains identical to the pre-cracked microstructure. The CISCC in lower Schmid factor grains primarily exhibits brittle fracture behavior. Extended deformation fields in lower Schmid factor grains originate exclusively from crack tip stresses and are accommodated by strain gradients and lattice rotations due to the less favorably oriented slip systems.
- Characteristic peanut-shaped distributions of GND densities are observed ahead of the crack tips (including mixed-mode cracks), representing the plastic zone morphology predicted by classical fracture mechanics theories. Such crack tip deformation fields and mixed-mode cracking indicate that CISC cracks are analogous to mechanically driven cracks.

Internal pitting is observed along CISC crack segments that undergo brittle fracture, with a distinct difference in the dislocation microstructure between the crack edge and the internal pit edges. Unlike the crack edges, the internal pit

edges are free of any plastic deformation, suggesting that the internal pits result from corrosion rather than fracture. The formation of internal pits can be correlated to stepwise crack propagation during brittle fracture. During an intermittent pause, the crack tip deformation field results in a higher dislocation density in the region, which promotes accelerated localized corrosion and leads to the formation of internal pits while crack propagation is paused.

Methods

Material

The test specimen used in this study was made from 3 mm-thick 304L stainless steel sheets. At first, 30° bevels were machined on sheet edges[58]. To mimic the vertical seam weld in SNF canisters, two-pass gas tungsten arc welding was used to assemble two beveled sheets with 308L stainless steel filler. The welding parameters were optimized to minimize bending during the welding. The chemical compositions of the stainless steel sheet and weld filler used in this study are provided in Table 1. Next, a 105 mm × 18.5 mm × 3 mm beam specimen was machined from the welded sheet, with the weld seam remaining lateral and centered along the beam axis. The schematic diagram of the beam specimen is shown in Fig. 12(a). Finally, this beam specimen was polished using SiC papers to flatten the weld bead, as is common industrial practice for SNF canisters.

Four-point bending test

To simulate the tensile residual stress at the vertical weld seams in SNF canisters, the beam specimen was strained using a four-point bending fixture. A loading bolt was used to apply the load, and loading continued until the maximum tensile

bending stress in the beam reached ~380 MPa[58]. The maximum tensile stress was estimated using equation 6 provided in ASTM G39[59]. We note that a slight difference in bending stress between the welded seam and the plate region was expected due to differences in mechanical properties. However, this difference was minimal and does not alter the observations in the present study. We also note that the region between the two loading points remained in pure bending, i.e., no shear stress acting in that region. Therefore, the crack initiation and propagation were free from any shear stress effect. After the beam specimen was strained, the loaded four-point bend fixture was aged in air for a few days prior to the corrosion tests.

Boiling $MgCl_2$ corrosion test

The corrosion in SNF canisters was emulated by boiling magnesium chloride ($MgCl_2$) test following ASTM G36[60]. The test was conducted at the Advanced Materials Laboratory at the University of New Mexico and at Sandia National Laboratories. The details of the corrosion test setup were provided in Qu and Wharry[61]. The loaded four-point bend fixture was fully immersed in the boiling solution throughout the test period. Reagent-grade magnesium chloride hexahydrate flakes and deionized (DI) water were used to prepare the boiling solution, with a $MgCl_2$ concentration of 54.3 wt%[62]. Throughout the test, the boiling solution temperature was maintained at 155±1 °C using a DI water-cooled condenser. The loaded four-point bend fixture was removed from the boiling solution every 2 hours for inspection. The test continued for approximately 17 hours. After that, the beam specimen was unloaded from the bending fixture, cleaned, and imaged as shown in Fig. 12(b).

Metallurgical preparation

After the corrosion test, a cuboid specimen was extracted from the beam specimen using a diamond circular saw. The approximate location of the cuboid specimen in the beam is highlighted in blue dashed lines in Fig. 12(a), which shows three microstructural regions: the welded region, the heat-affected zone, and the base metal. In the current example, the CISC crack propagated through the outer heat-affected zone, which has an equiaxed grain structure similar to the base metal and is free of extreme sensitization and/or the dendritic microstructure of the inner heat-affected zone[17,26,63]. To investigate the CISC crack propagation path, the cuboid surface parallel to the beam specimen's transverse direction (TD) was prepared for microstructural characterization. To achieve optimal edge retention during metallographic polishing, the specimen was first mounted in a graphite-blend conductive resin. For metallographic surface preparation, a Buehler EcoMet30 semi-automated polishing system was used. The surface was ground with gradually finer SiC papers up to 1200 grit, followed by polishing with 6 μm, 3 μm, and 1 μm diamond suspension. After this, the specimen was polished using a vibratory polisher with 0.05 colloidal silica for 24 hours, which resulted in a mirror-like surface suitable for HR-EBSD analysis. Subsequently, the specimen was ultrasonically cleaned in a micro-organic soap solution, followed by isopropanol, for 10 minutes each. This step ensures the removal of any residual silica particles from the surface.

HR-EBSD

The HR-EBSD data acquisition was performed using a Helios G4 UX FEG dual beam SEM equipped with an Oxford Symmetry S3 EBSD detector at the Birck Nanotechnology Center at Purdue University. Highly localized deformation fields (e.g., near the crack tip) significantly degrade the quality of the Kikuchi pattern due to dislocation-induced incoherent scattering and the presence of elastic gradients. To mitigate this, the geometric and electron beam parameters were optimized. In this study, the Kikuchi patterns were captured at 16-bit depth and 1244 × 1024 resolution with both static and dynamic background corrections. An accelerating voltage of 30 kV, a beam current of 6 nA, and an exposure time of 1.5 ms were used to capture Kikuchi patterns at a 250 nm step size without binning. The final high-quality Kikuchi patterns were obtained by averaging 30 frames each pixel. Instead of using a longer exposure time, frame averaging was used to avoid saturation caused by the high yield in CMOS detectors.

Once the Kikuchi patterns were collected, the HR-EBSD analysis was performed using Crosscourt4 (CC4) software by BLG·Vantage. An automated reference pattern selection algorithm was used to select reference Kikuchi patterns in each grain with a 5° reference tolerance angle[29]. We note that this algorithm selects the highest-quality Kikuchi pattern in a grain as the reference, typically from the region with the fewest defects. For the HR-EBSD analysis, 256 × 256-pixel regions of interest (ROIs) were extracted from each individual Kikuchi pattern and correlated with the reference pattern from the corresponding grain using an FFT-based cross-correlation technique. A remapping pass was used to remove large rigid rotations and translations of Kikuchi patterns that resulted from crack tip deformation[64]. Following this, the high-resolution kernel average

misorientation (HR-KAM), GND density, and relative elastic strains were estimated for each dataset.

cECCI

In the present study, ECCI was carried out under controlled diffraction conditions. For this purpose, conventional EBSD and Electron Channeling Pattern (ECP) analysis were first performed on a single crystal Si reference to calibrate the stage movements, and then at selected crack tip regions. Further, the Kikuchi patterns and ECPs obtained from this analysis were analyzed using the *openECCI* package[65] to estimate optimal channeling conditions (i.e., stage tilt and rotation) for different grains of interest near the crack tip. Once the channeling conditions were achieved, dislocation imaging was performed using a Thermo Fisher Scientific Apreo II scanning electron microscope equipped with a directional backscatter detector at the Center for Electron Microscopy and Analysis (CEMAS) at Ohio State University. An accelerating voltage of 20 kV and a beam current of 13 nA were used for imaging. Alongside, a pixel width of 3.37 nm was optimized to accurately resolve the dislocation microstructure and was maintained across all micrographs.

Funding declaration

R.R. and J.W. declare that the research reported in this work was supported by the U.S. Department of Energy Office of Nuclear Energy (DOE, NE) through Contract No. DE, NE0009389.

Table(s)

Table 1 – Chemical composition of the base material and weld filler.

Alloys		Alloying elements in wt.%										
		Fe	C	Si	Cr	P	S	N	Mn	Ni	Mo	Cu
Base material	S30403	Bal.	0.027	0.35	18.11	0.023	0.04	0.056	1.31	8.02	–	–
Weld filler	S30880	Bal.	0.014	0.47	19.88	0.021	0.002	–	1.83	9.66	0.01	0.1

Figures

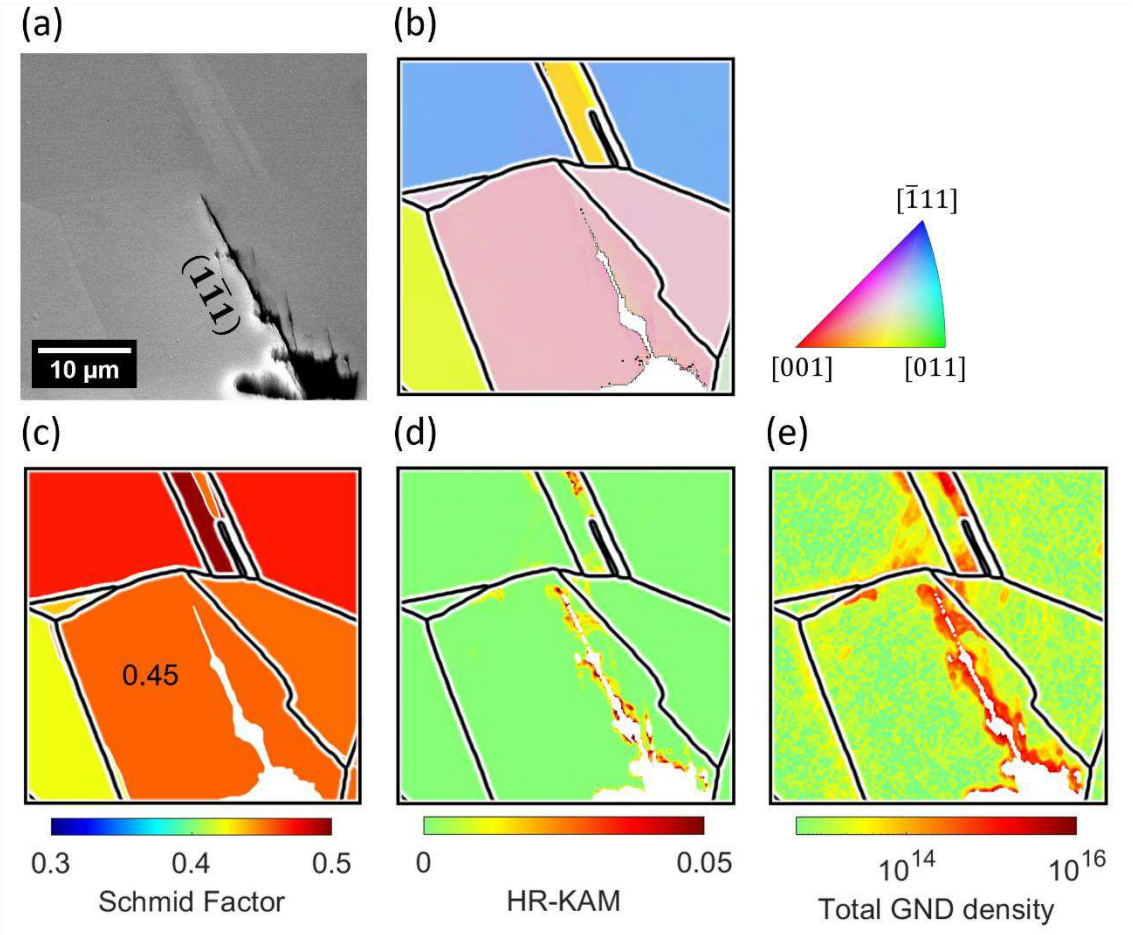


Fig. 1 – CISC crack propagating through a lower Schmid factor grain. Due to localized corrosion, internal pits along the crack path are formed at the locations where crack propagation is discontinued. (a) Secondary electron image, (b) Inverse pole figure along Z-axis, (c) Schmid factor in different grains, (d) High-resolution kernel average misorientation map in rads, and (e) Total GND density map in $\log_{10} \mathrm{m}^{-2}$.

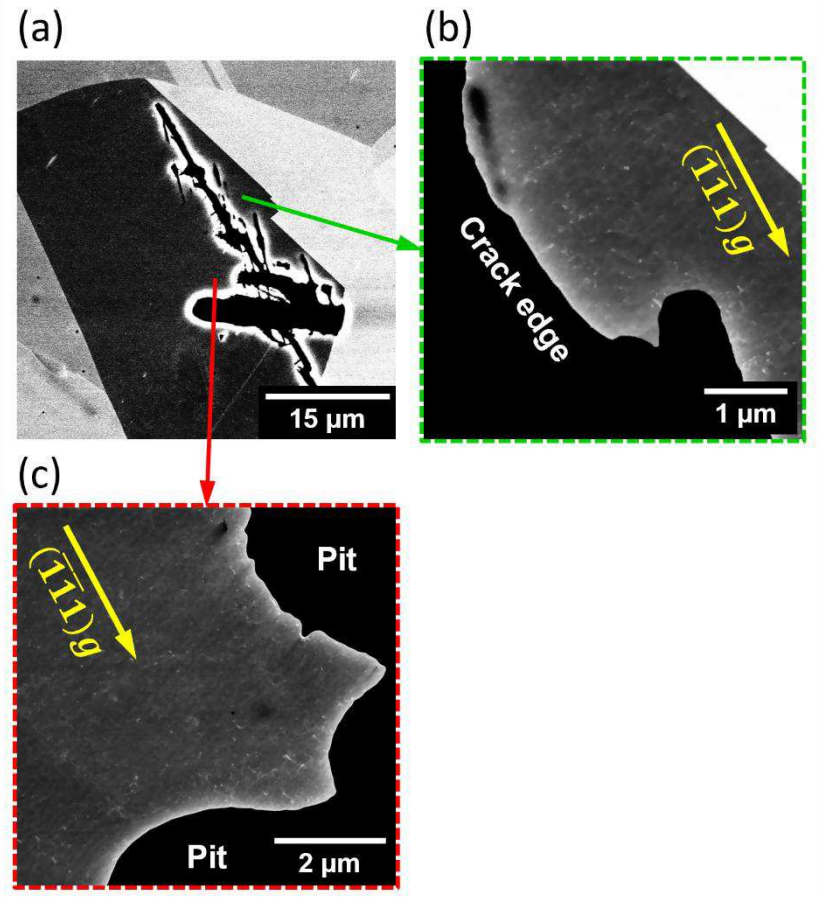


Fig. 2 – (a) ECC Image exhibiting distribution of dislocations around a crack propagating through a lower Schmid factor grain during CISCC (corresponding to data shown in Fig. 1). (b) ECC image near the crack edge showing relatively higher dislocation density, (c) ECC image around internal pits with comparatively lower dislocation density.

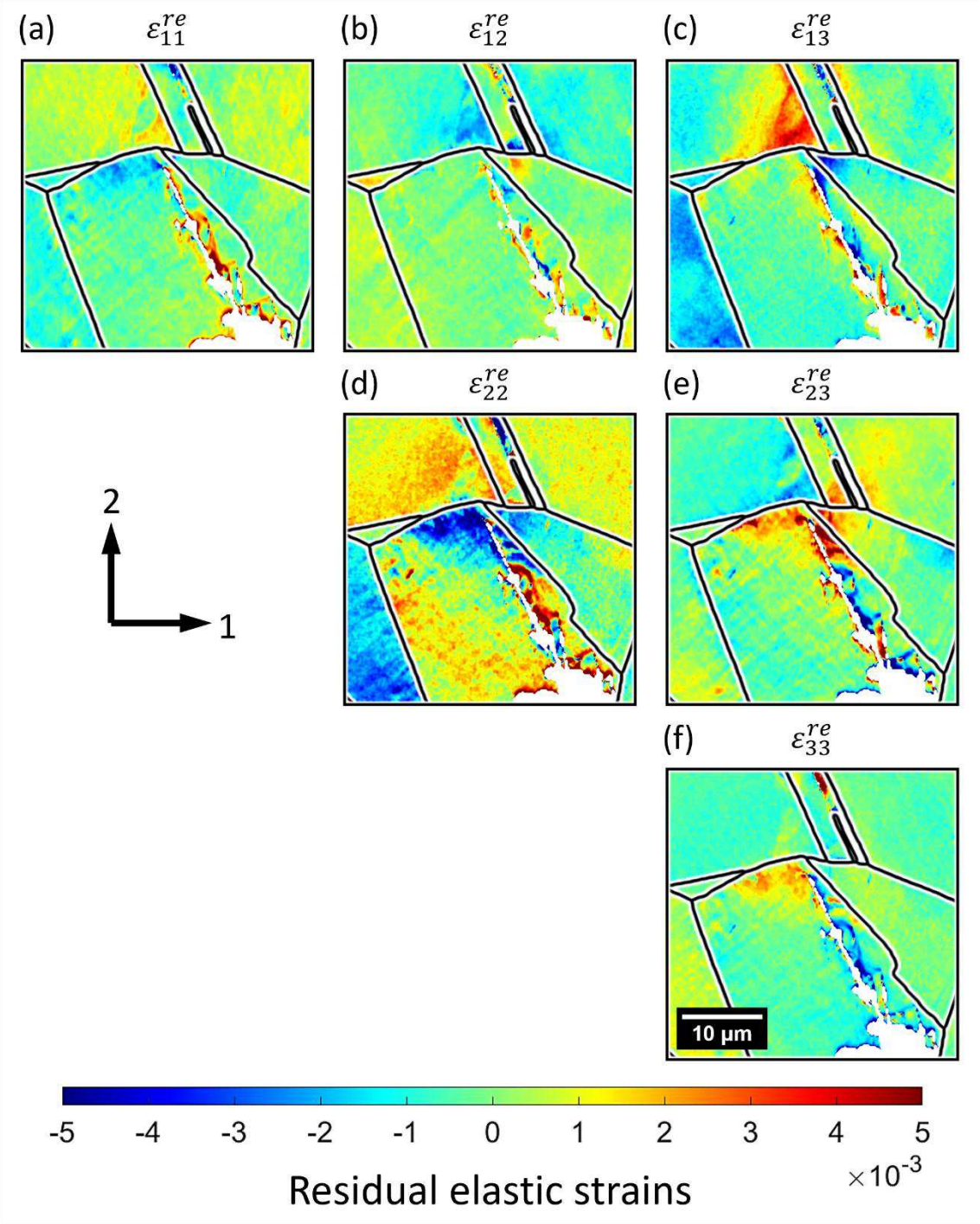


Fig. 3 – Residual elastic strain components around a crack propagating through a lower Schmid factor grain during CISCC (corresponding to data shown in Fig. 1). (a) ε_{11}^{re}, (b) ε_{12}^{re}, (c) ε_{13}^{re}, (d) ε_{22}^{re}, (e) ε_{23}^{re}, and (f) ε_{33}^{re}.

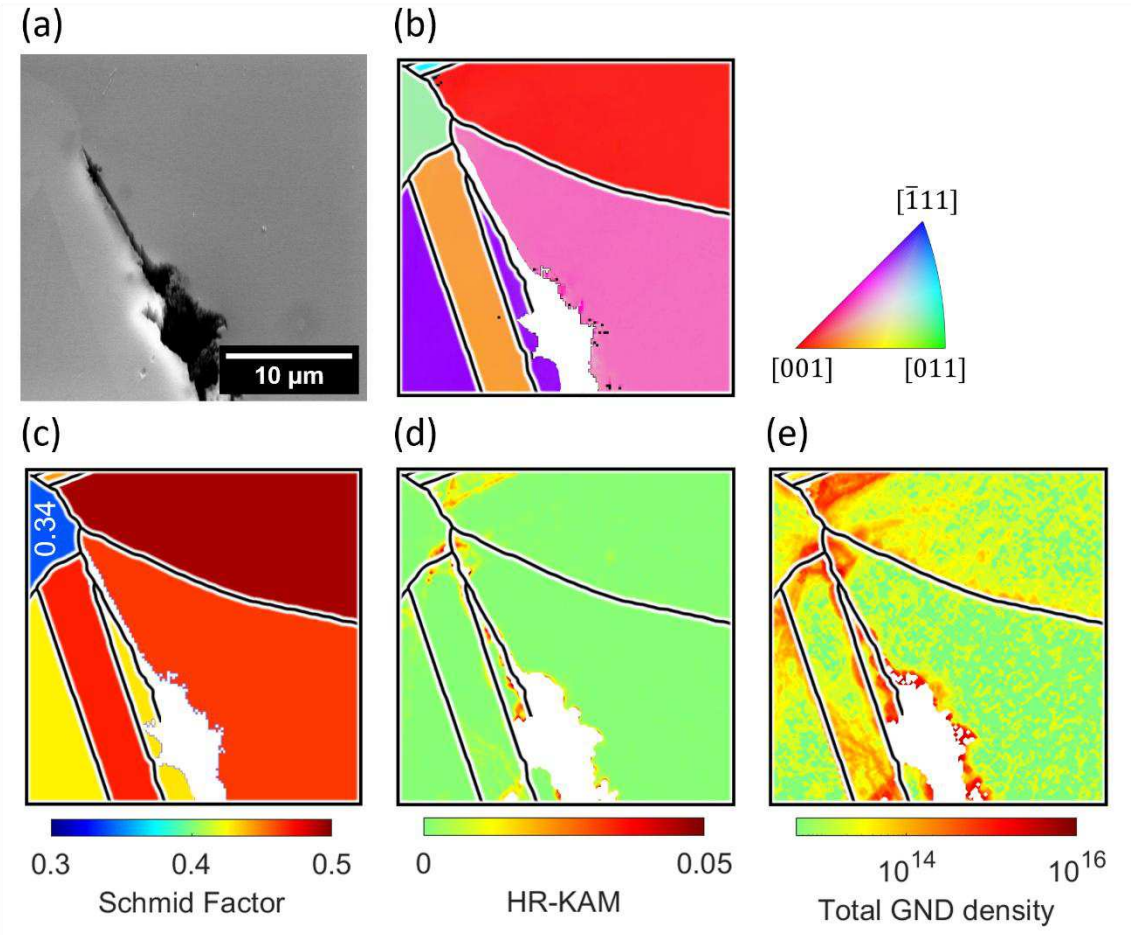


Fig. 4 – Intergranular cracking during CISCC. An internal pit along the crack path was formed while the crack paused at that location. (a) Secondary electron image, (b) Inverse pole figure along Z-axis, (c) Schmid factor in different grains, (d) High-resolution kernel average misorientation map in rads, and (e) Total GND density map in $\log_{10} \mathrm{m}^{-2}$.

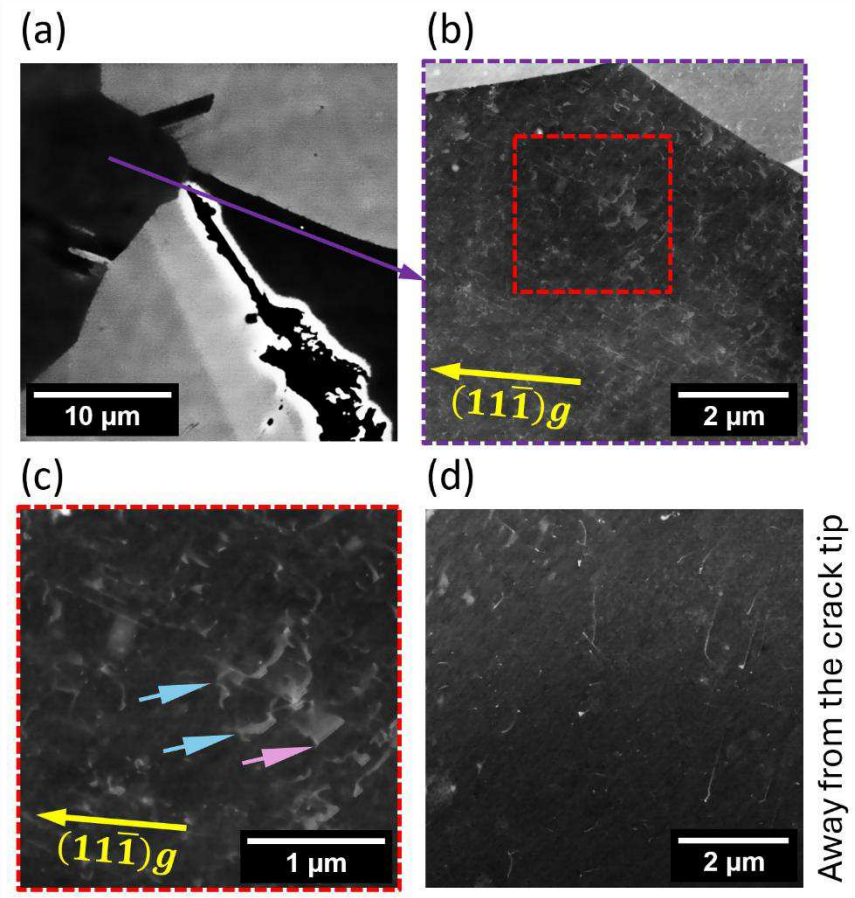


Fig. 5 – (a) ECC Image exhibiting taken at the tip of the intergranular crack (corresponding to data shown in Fig. 4). (b) ECC image at the crack tip grain shows significant dislocation activity, (c) High magnification ECC image focusing on different dislocation characteristics, stacking fault (pink arrow) and dislocation partials (sky arrow). (d) ECC image away from the crack tip representing the initial dislocation density in the material.

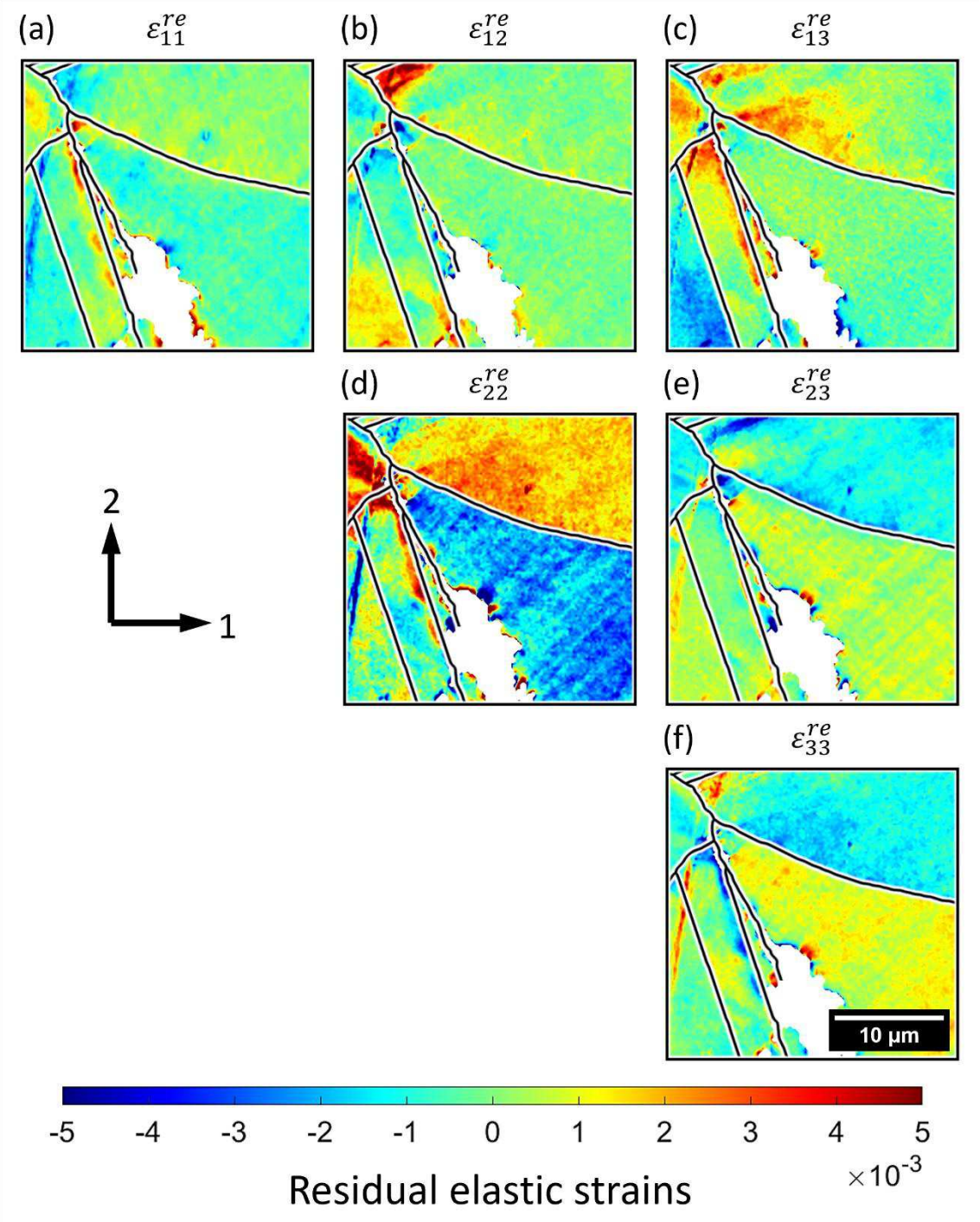


Fig. 6 – Residual elastic strain components around the crack tip of the intergranular CISC crack shown in Fig. 4. (a) ε_{11}^{re}, (b) ε_{12}^{re}, (c) ε_{13}^{re}, (d) ε_{22}^{re}, (e) ε_{23}^{re}, and (f) ε_{33}^{re}.

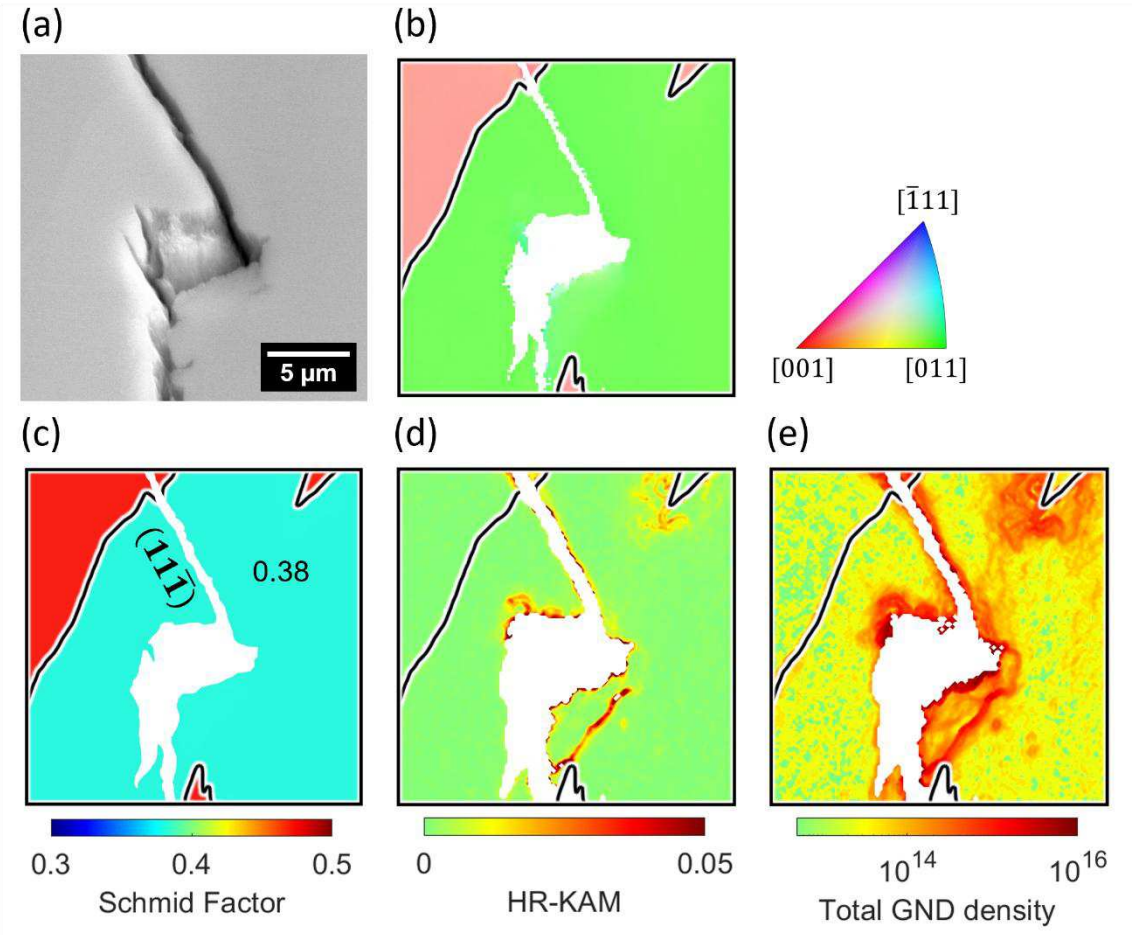


Fig. 7 – Internal pit on a previously grown CISC crack path. (a) Secondary electron image, (b) Inverse pole figure along Z-axis, (c) Schmid factor in different grains, (d) High-resolution kernel average misorientation map in rads, and (e) Total GND density map in $\log_{10} \mathrm{m}^{-2}$.

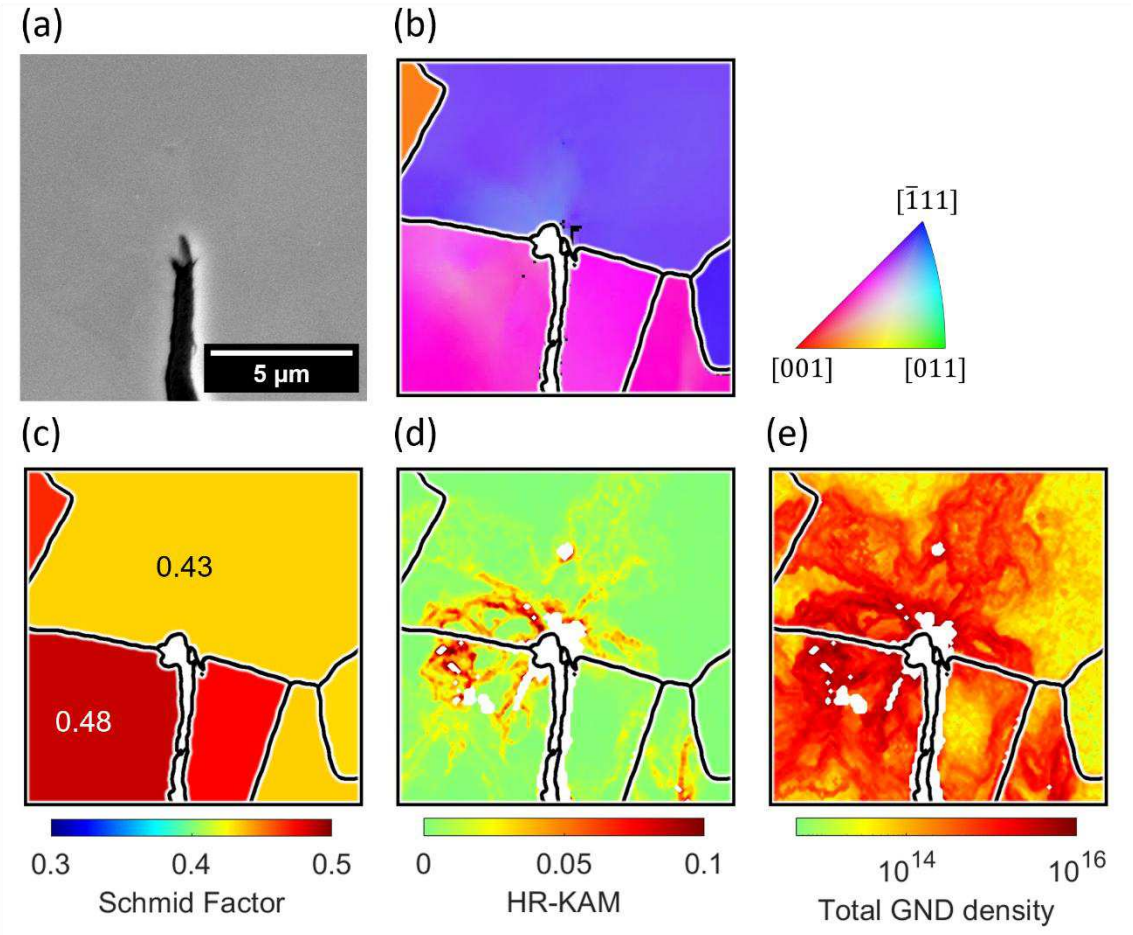


Fig. 8 – CISC crack propagating through a higher Schmid factor grain. (a) Secondary electron image, (b) Inverse pole figure along Z-axis, (c) Schmid factor in different grains, (d) High-resolution kernel average misorientation map in rads, and (e) Total GND density map in $\log_{10} \mathrm{m}^{-2}$**.**

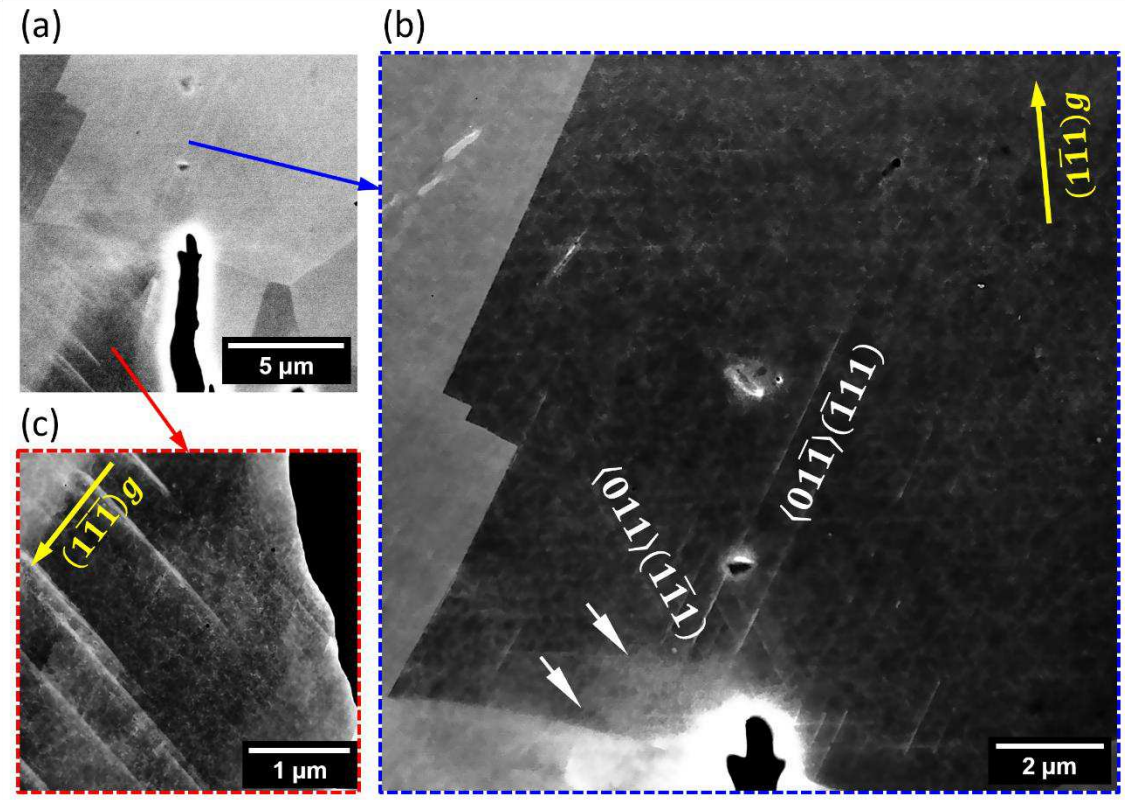


Fig. 9 – (a) ECC Image exhibiting distribution of dislocations around propagating through a higher Schmid factor grain during CISCC (corresponding to data shown in Fig. 8). (b) Enlarged ECC image at the crack tip showing significant plastic deformation near to the crack tip (marked with white arrows) and activation of different slip systems onset of the crack tip (c) ECC image taken along the crack edge showing significant dislocation activity.

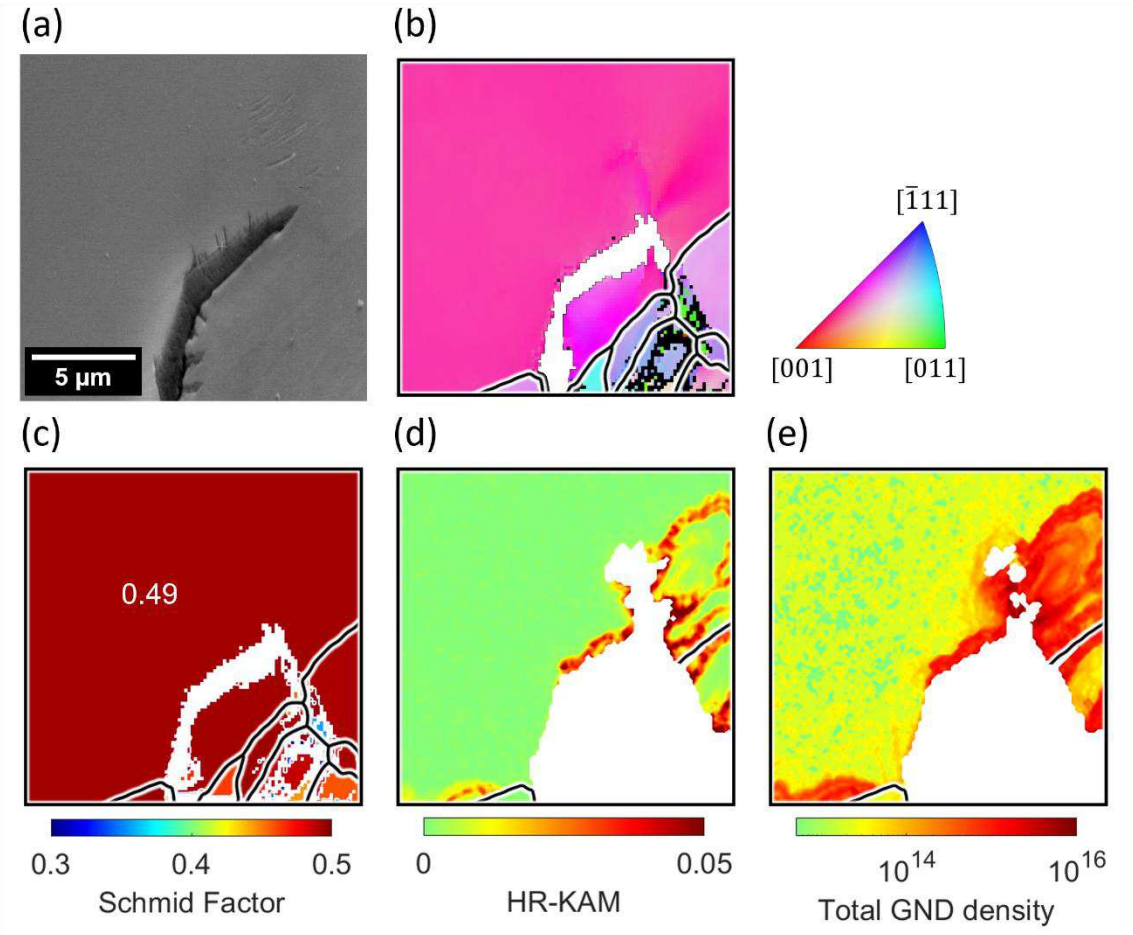


Fig. 10 – CISC crack propagating through a higher Schmid factor grain. (a) Secondary electron image, (b) Inverse pole figure along Z-axis, (c) Schmid factor in different grains, (d) High-resolution kernel average misorientation map in rads, and (e) Total GND density map in $\log_{10} \mathrm{m}^{-2}$.

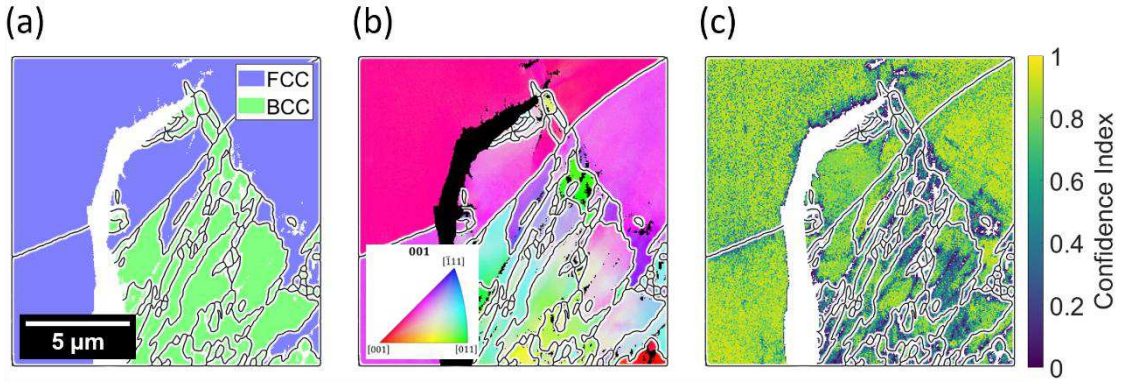


Fig. 11 – Stress-induced martensite transformation adjacent to the crack path (corresponding to the data presented in Fig. 10). (a) Phase map, (b) Inverse pole figure along Z-axis, and (c) Confidence index map corresponds to the Hough transform of the dataset.

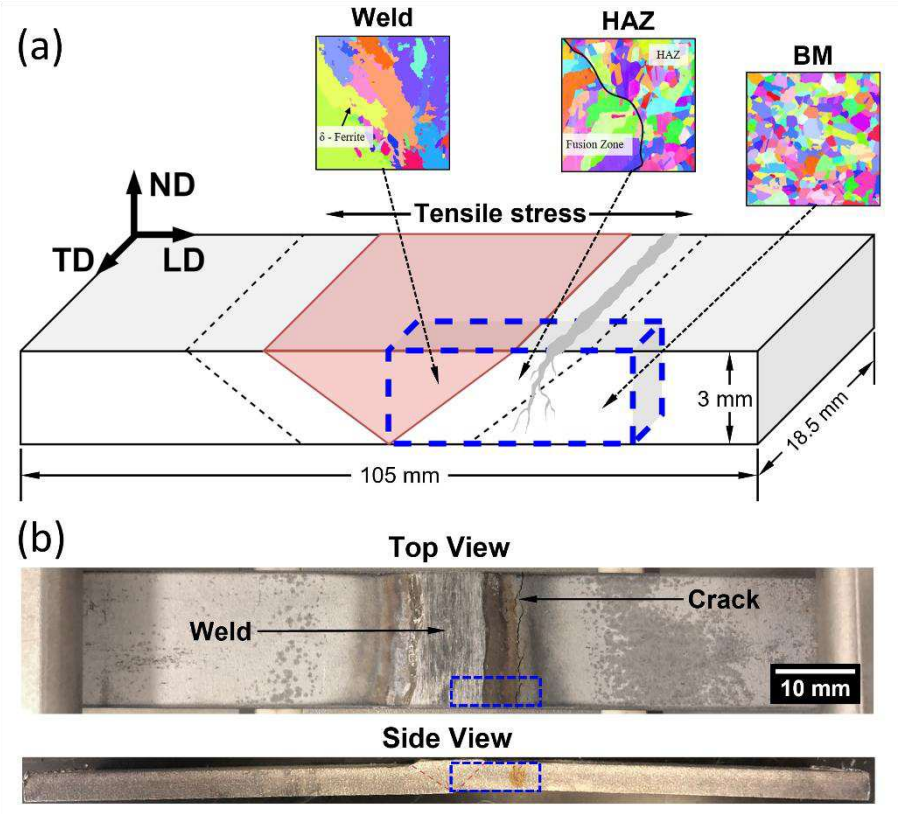


Fig. 12 – (a) Schematic diagram of the welded specimen with dimensions. The inset provides EBSD micrographs relevant to each welded, HAZ, and base metal (BM) region. (b) Top and side views after the corrosion test. Characterization is conducted in the region marked by a blue dashed cuboid. Adapted from [9], through Creative Commons Attribution 4.0 International License.

References

1. Park, I., Kim, E.-Y. & Yang, W.-J. Microstructural investigation of stress corrosion cracking in cold-formed AISI 304 reactor. *Metals (Basel).* **11**, 7 (2020).

2. Vakili, M., Koutník, P., Kohout, J. & Gholami, Z. Analysis, Assessment, and Mitigation of Stress Corrosion Cracking in Austenitic Stainless Steels in the Oil and Gas Sector: A Review. *Surfaces (2571-9637)* **7**, (2024).

3. Fujimori, H. *et al.* Stress corrosion cracking in light water reactors: good practices and lessons learned. *International Atomic Energy Agency, Vienna, Austria, Report No. NP* (2011).

4. McCafferty, E. *Introduction to Corrosion Science*. vol. 236 (Springer, 2010).

5. Martin, U. & Bastidas, D. M. Stress corrosion cracking failure analysis of AISI 1018 carbon steel reinforcing bars in carbonated and chloride contaminated environment. *Eng. Fail. Anal.* **147**, 107159 (2023).

6. Rahimi, S. & Marrow, T. J. A new method for predicting susceptibility of austenitic stainless steels to intergranular stress corrosion cracking. *Mater. Des.* **187**, 108368 (2020).

7. Alyousif, O. M. & Nishimura, R. The stress corrosion cracking behavior of austenitic stainless steels in boiling magnesium chloride solutions. *Corros. Sci.* **49**, 3040–3051 (2007).

8. Lu, B. T., Chen, Z. K., Luo, J. L., Patchett, B. M. & Xu, Z. H. Pitting and stress corrosion cracking behavior in welded austenitic stainless steel. *Electrochim. Acta* **50**, 1391–1403 (2005).

9. Qu, H. J. *et al.* Crystallographic effects on transgranular chloride-induced stress corrosion crack propagation of arc welded austenitic stainless steel. *Npj Mater. Degrad.* **6**, 43 (2022).

10. Qiao, L. J., Gao, K. W., Volinsky, A. A. & Li, X. Y. Discontinuous surface cracks during stress corrosion cracking of stainless steel single crystal. *Corros. Sci.* **53**, 3509–3514 (2011).

11. Turnbull, A., McCartney, L. N. & Zhou, S. Modelling of the evolution of stress corrosion cracks from corrosion pits. *Scr. Mater.* **54**, 575–578 (2006).

12. Turnbull, A., McCartney, L. N. & Zhou, S. A model to predict the evolution of pitting corrosion and the pit-to-crack transition incorporating statistically distributed input parameters. in *Environment-induced cracking of materials* 19–45 (Elsevier, 2008).

13. Panda, B., Sujata, M., Madan, M. & Bhaumik, S. K. Stress corrosion cracking in 316L stainless steel bellows of a pressure safety valve. *Eng. Fail. Anal.* **36**, 379–389 (2014).

14. Kumar, M. S., Sujata, M., Venkataswamy, M. A. & Bhaumik, S. K. Failure analysis of a stainless steel pipeline. *Eng. Fail. Anal.* **15**, 497–504 (2008).

15. Spencer, D. T. *et al.* The initiation and propagation of chloride-induced transgranular stress-corrosion cracking (TGSCC) of 304L austenitic stainless steel under atmospheric conditions. *Corros. Sci.* **88**, 76–88 (2014).

16. Tani, J., Mayuzumi, M. & Hara, N. Stress corrosion cracking of stainless-steel canister for concrete cask storage of spent fuel. *Journal of Nuclear Materials* **379**, 42–47 (2008).

17. Xie, Y. & Zhang, J. Chloride-induced stress corrosion cracking of used nuclear fuel welded stainless steel canisters: A review. *Journal of Nuclear Materials* **466**, 85–93 (2015).

18. Qu, H. J., Tatman, J. & Wharry, J. P. Chloride-induced stress corrosion cracking in Austenitic steels for SNF storage canisters-Recent understanding and advances in mitigation and repair. *Journal of Nuclear Materials* 155080 (2024).

19. Qu, H. J. *et al.* Stress corrosion cracking mechanism of cold spray coating on a galvanically similar substrate. *Materials Science and Engineering: A* **849**, 143404 (2022).

20. Katona, R. M., Karasz, E. K. & Schaller, R. F. A review of the governing factors in pit-to-crack transitions of metallic structures. *Corrosion* **79**, 72–96 (2023).

21. Schoell, R. *et al.* In situ synchrotron X-ray tomography of 304 stainless steels undergoing chlorine-induced stress corrosion cracking. *Corros. Sci.* **170**, 108687 (2020).

22. Schoell, R. *et al.* Mechanism of chlorine-induced stress corrosion cracking of two 304 SS heats in simulated marine environment through in situ X-ray tomography and diffraction: Role of deformation induced martensite and crack branching. *Mater. Charact.* **190**, 112020 (2022).

23. Wang, C. *et al.* Microstructure evolution and corrosion behavior of dissimilar 304/430 stainless steel welded joints. *J. Manuf. Process.* **50**, 183–191 (2020).

24. Alyousif, O. M. & Nishimura, R. On the stress corrosion cracking and hydrogen embrittlement behavior of austenitic stainless steels in boiling saturated magnesium chloride solutions. *International Journal of Corrosion* **2012**, 462945 (2012).

25. Martin, U., Birbilis, N., Macdonald, D. D. & Bastidas, D. M. Pit-to-crack mechanisms of 316LN stainless steel reinforcement in alkaline solution influenced by strain induced martensite. *Npj Mater. Degrad.* **7**, 88 (2023).

26. Roy, R., Qu, H. J., Mao, K. S. & Wharry, J. P. Chloride-induced stress corrosion crack propagation mechanisms in austenitic stainless steel are mechanically driven. *Scr. Mater.* **262**, 116652 (2025).

27. Wilkinson, A. J., Meaden, G. & Dingley, D. J. High resolution mapping of strains and rotations using electron backscatter diffraction. *Materials Science and Technology* **22**, 1271–1278 (2006).

28. Wilkinson, A. J., Meaden, G. & Dingley, D. J. High-resolution elastic strain measurement from electron backscatter diffraction patterns: New levels of sensitivity. *Ultramicroscopy* **106**, 307–313 (2006).

29. Britton, T. B. & Wilkinson, A. J. Measurement of residual elastic strain and lattice rotations with high resolution electron backscatter diffraction. *Ultramicroscopy* **111**, 1395–1404 (2011).

30. Britton, T. B. & Hickey, J. L. R. Understanding deformation with high angular resolution electron backscatter diffraction (HR-EBSD). *IOP Conf. Ser. Mater. Sci. Eng.* **304**, 012003 (2018).

31. Roy, R., Long, F., Moore, B. & Daymond, M. R. Creep-induced microstructures in Zircaloy-4: comparing thermal and irradiation creep. *Acta Mater.* **297**, 121370 (2025).

32. Koko, A. *et al.* HR-EBSD analysis of in situ stable crack growth at the micron scale. *J. Mech. Phys. Solids* **172**, 105173 (2023).

33. Ast, J., Polyakov, M. N., Mohanty, G., Michler, J. & Maeder, X. Interplay of stresses, plasticity at crack tips and small sample dimensions revealed by in-situ microcantilever tests in tungsten. *Materials Science and Engineering: A* **710**, 400–412 (2018).

34. Roy, R., Shaik, A., Topping, M., Long, F. & Daymond, M. R. Investigation of fine-scale dislocation distributions at complex geometrical structures by using HR-EBSD and a comparison with conventional EBSD. *Mater. Charact.* **207**, 113498 (2024).

35. Ruggles, T. J., Gilliland, W. G., Fullwood, D. T. & Kacher, J. An overview of HR-EBSD techniques for mapping local stress and dislocations in crystalline materials at sub-micron resolution. *Prog. Mater. Sci.* 101585 (2025).

36. Phillips, N. W. *et al.* Nanoscale lattice strains in self-ion implanted tungsten. *Acta Mater.* **195**, 219–228 (2020).

37. Yu, H. *et al.* New perspectives on collision cascade damage in self-ion irradiated tungsten from HR-EBSD and ECCI. *Journal of Nuclear Materials* **554**, 153074 (2021).

38. Roy, R., Long, F. & Daymond, M. R. A mechanistic study of grain boundary behaviour during irradiation-induced growth in zirconium. *Acta Mater.* **276**, 120075 (2024).

39. Zaefferer, S. & Elhami, N.-N. Theory and application of electron channelling contrast imaging under controlled diffraction conditions. *Acta Mater.* **75**, 20–50 (2014).

40. Kriaa, H., Guitton, A. & Maloufi, N. Fundamental and experimental aspects of diffraction for characterizing dislocations by electron channeling contrast imaging in scanning electron microscope. *Sci. Rep.* **7**, 9742 (2017).

41. Schmid, E. Yield point of crystals, critical shear stress law. in *Proceedings of the First International Congress for Applied Mechanics, Delft* vol. 342 (1924).

42. Nye, J. F. Some geometrical relations in dislocated crystals. *Acta Metallurgica* **1**, 153–162 (1953).

43. Skippon, T., Balogh, L. & Daymond, M. R. Comparison of electron backscatter and X-ray diffraction techniques for measuring dislocation density in Zircaloy-2. *J. Appl. Crystallogr.* **52**, 415–427 (2019).

44. Jiang, J., Britton, T. B. & Wilkinson, A. J. Evolution of intragranular stresses and dislocation densities during cyclic deformation of polycrystalline copper. *Acta Mater.* **94**, 193–204 (2015).

45. Britton, T. B. & Wilkinson, A. J. Stress fields and geometrically necessary dislocation density distributions near the head of a blocked slip band. *Acta Mater.* **60**, 5773–5782 (2012).

46. Zhang, T., Jiang, J., Shollock, B. A., Britton, T. Ben & Dunne, F. P. E. Slip localization and fatigue crack nucleation near a non-metallic inclusion in polycrystalline nickel-based superalloy. *Materials Science and Engineering: A* **641**, 328–339 (2015).

47. Roy, R., Topping, M. & Daymond, M. R. In-situ assessment of microscale crack tip fields in zirconium. *Int. J. Mech. Sci.* **264**, 108812 (2024).

48. Roy, R., Long, F. & Daymond, M. R. Evaluation of deformation fields associated with irradiation-induced growth and grain boundary interactions in zirconium. *Materialia (Oxf).* **39**, 102325 (2025).

49. Wakinaga, R. *et al.* Crystal Orientation Analysis on Stress Corrosion Cracking Facets in Austenitic Stainless Steels. *Key Eng. Mater.* **810**, 64–69 (2019).

50. Anderson, T. L. *Fracture Mechanics*. (CRC Press, 2017). doi:10.1201/9781315370293.

51. Singh Raman, R. K. & Pal, S. A simple approach to the determination of threshold stress intensity for stress corrosion cracking (K ISCC) and crack growth of sensitized austenitic stainless steel. *Metallurgical and Materials Transactions A* **42**, 2643–2651 (2011).

52. Bjerkén, C. & Melin, S. A study of the influence of grain boundaries on short crack growth during varying load using a dislocation technique. *Eng. Fract. Mech.* **71**, 2215–2227 (2004).

53. Liu, Z.-E. & Wei, Y. An analytical solution to the stress fields of kinked cracks. *J. Mech. Phys. Solids* **156**, 104619 (2021).

54. Torbati-Sarraf, H., Qu, H., Wharry, J. P. & Chawla, N. Internal pitting on chloride-induced stress corrosion cracks in 304 L stainless steel weldment revealed by X-ray microcomputed tomography. *Mater. Charact.* 116442 (2026).

55. Griffith, A. A. The phenomena of rupture and flow in solids. *Philosophical Transactions of the Royal Society of London. Series A, Containing Papers of a Mathematical or Physical Character* **221**, 163–198 (1921).

56. Stanisławska, A. *et al.* Influence of laser powder bed fusion build orientation on the corrosion resistance of CoCrWMo alloy considering dislocation density character and lattice microstrain. *Sci. Rep.* (2025).

57. Fontana, M. G. Corrosion engineering. (1985).

58. Enos, D. & Bryan, C. R. *Characterization of Canister Mockup Weld Residual Stresses*. (2016).

59. *ASTM G39-99 Standard Practice for Preparation and Use of Bent-Beam Stress-Corrosion Test Specimens*. www.astm.org (2021) doi:10.1520/G0039-99R21.

60. ASTM G36-24 Practice for Evaluating Stress-Corrosion-Cracking Resistance of Metals and Alloys in a Boiling Magnesium Chloride Solution. Preprint at https://doi.org/10.1520/G0036-24 (2024).

61. Qu, H. J. & Wharry, J. P. Crystallographic orientation data from chloride-induced stress corrosion crack (CISCC) paths in gas tungsten arc welded (GTAW) austenitic stainless steel 304L. *Data Brief* **42**, 108059 (2022).

62. Casale, I. B. Boiling temperatures of mg cl solutions-their application in stress corrosion studies. *Corrosion* **23**, 314–317 (1967).

63. Dong, P., Scatigno, G. G. & Wenman, M. R. Effect of salt composition and microstructure on stress corrosion cracking of 316L austenitic stainless steel for dry storage canisters. *Journal of Nuclear Materials* **545**, 152572 (2021).

64. Britton, T. B. & Wilkinson, A. J. High resolution electron backscatter diffraction measurements of elastic strain variations in the presence of larger lattice rotations. *Ultramicroscopy* **114**, 82–95 (2012).

65. Xu, Z., Ånes, H. W., Gorelick, S., Fang, X. & Miller, P. IMBalENce/openECCI: v 0.1.0 First release. Preprint at https://doi.org/10.5281/zenodo.11183730 (2024).